Travelling Perversion as Constant Torque Actuator

Émilien Dilly, Sébastien Neukirch, Julien Derr, Dražen Zanchi

Travelling Perversion as Constant Torque Actuator

Émilien Dilly,[1] Sébastien Neukirch,[2] Julien Derr,[3] and Dražen Zanchi[1,*]

[1] *Laboratoire Matière et Systèmes Complexes, UMR 7057, Université Paris Cité, CNRS, F-75205 Paris Cedex 13, France*

[2] *Institut Jean Le Rond d'Alembert, CNRS (UMR 7190), Sorbonne Université, 75005 Paris, France*

[3] *Laboratoire Reproduction et Développement des Plantes, Ecole Normale Supérieure de Lyon, CNRS, 69364 Lyon Cedex 07, France*

(Date : 13 avril 2023)

Mechanical stress and conformation of helical elastic rod clamped at both ends were studied upon unwinding process. By axial rotation of one end, the winding number was progressively changed from the natural one ($n = n_0$) to complete chirality inversion ($n = -n_0$) while keeping the total elongation fixed and monitoring the applied torque M and tension T. Along the unwinding, the system crosses three well distinguished states : natural helix (+), mixed state (+/-) and inverted helix (-). The mixed state involves two helices with opposite chiralities spatially connected by a perversion (helicity inversion). Upon unwinding the perversion is first "injected" (nucleated) from one side, travels towards the opposite side where it finally gets "absorbed" (annihilated), leaving the system in the (-) state. In the mixed state the profile of $M(n)$ is almost flat : the system behaves as a constant torque actuator. The three states are quantitatively well described in the framework of a biphasic model, neglecting the perversion energy and finite size effects. The latter are taken into account in a numerical simulation based on the Kirchhoff theory of elastic rods. It reproduces the clamped rod conformations and the observed profiles $M(n)$ and $T(n)$, including abrupt jumps at nucleation and annihilation of the perversion.

The interest for twisted elastic rods [1–3] was renewed in the last decades [4, 5] in the context of single molecule DNA nano-mechanics [6–11], plant development [12, 13], soft robotics, or micro-engineering applications [14–16], and these applications have in turn motivated theoretical research [17–22].

An unloaded elastic rod which is homogeneously *curved* and *twisted* adopts a helical shape with radius R_0 and pitch χP_0, with chirality $\chi = \pm 1$ for positively/negatively turning helix corresponding to positive/negative winding number (topological link) n_0. If the rod is now held by its ends and twisted in such a way that the total winding number n is reduced to zero, its shape then comprises two helices with opposite handedness separated by an inversion called perversion, a phenomenon relevant for a number of biological and bio-inspired systems including tendrils of plants [23, 24], propelling flagella of microorganisms [25, 26] and even electrospun micro-fibrils [27, 28]. Theoretical description of helical elastic rods is a particularly elegant application of dynamical systems formalism and is often offered as explanation of winding of tendrils of plants with single or multiple perversions [29–31].

It was recently proposed that perversions in elastic helical ribbon can be related by analogy to fractional charges Haldane's dimerized quantum spin chain [22]. However analysis of the complete handedness inversion of an elastic helix is, to our knowledge, still an open question from both experimental and theoretical point of views. To reverse the chirality of a helix with $n = n_0$, one can start to unwind it at constant elongation (see Fig.1 (a) and supplemental video 1). At some critical winding $n < n_0$ a perversion is generated at one end, in agreement with theoretical prediction [22]. As unwinding continues, the injected perversion travels toward the opposite end. Finally, as $n \simeq -n_0$, the perversion gets "absorbed" at the opposite end and we obtain a purely hand-reversed helix. If now the stretching force is relieved, the elongation decreases and the obtained hand-reversed helix adopts a conformation where the coils are collapsed, maintained by contact forces (see supplementary Fig. S1).

We report on experiments on chirality inversion of elastic helical rods. The rod was clamped at both ends and for different elongations, we monitored the axial torque M and axial force T as functions of the winding number n, from $n = n_0$ to $n = -n_0$, see Fig. 2. This enabled us to infer a phase diagram for three encountered phases, the natural chirality helix (+), the coexistence of both chiralities (+/−) and the opposite chirality (−), see Fig.1 (b). The phase diagram is reproduced within a model based on phase coexistence of just the (+) and (-) chirality helices ignoring clamped boundaries and the perversion. In order to take into account the perversion itself and boundary conditions, we performed full numerical simulations on a finite-size system. As result, we reproduced the jump at transition and details of force and torque profiles $T(n)$ and $M(n)$ across the inversion transition.

Helical rods were moulded of two-component elastomer (Wagner Silicones AWASIL NOVO 90). After mixing, the two reactants are loaded into a syringe with nozzle diameter d and extruded to a helical shape by deposition on a cylinder with a desired radius and pitch. Once curing is reached, the rods have a permanent helical state. A Young modulus of $E = 5.0 \pm 2$ MPa is measured from a simple cantilever beam experiment and the value of $\nu = 0.5$ for the Poisson ratio is assumed, typical for elastomers. We present in this letter data for a helix ha-

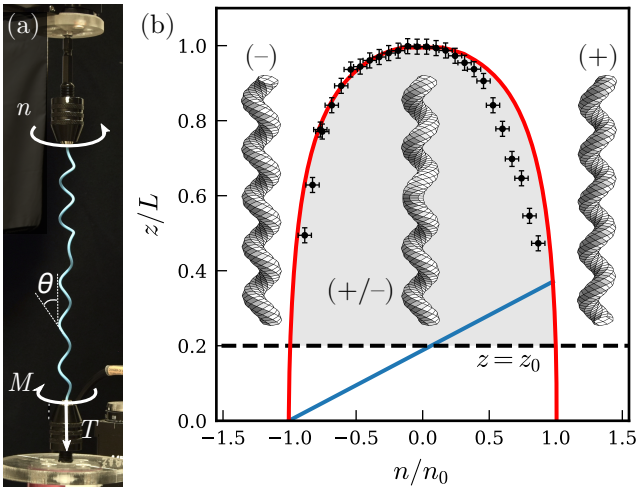

FIGURE 1. (a) : Experimental setup ; the rod is held by mandrels at its extremities, the upper mandrel is rotated n turns while the lower mandrel is fixed to a torque-meter and a scale. The mandrels apply a torque $\mathbf{M}$ and a force $\mathbf{T}$ on the rod. (b) : Experimental phase diagram in the $(\tilde{z}, \tilde{n})$ plane for the parameter value $z_0/L = 0.2$, where L is the total length. The regions $(-)$, $(+/-)$ and $(+)$ correspond respectively to reversed chirality, coexistence of both chiralities and natural chirality. The dotted horizontal line for $z = z_0$ represents the value of z of the unloaded helix, so that for $z > z_0$ (shaded) the helix is extended. The black crosses are experimental data and the red curve is the calculated phase boundary. The blue line is the calculated limit below which the $(-)$ part of the rod has loops collapsed in self-contact.

ving radius $R_0 = 3.9$ mm, pitch $P_0 = 4.7$ mm, thickness $d = 1.7$ mm and $n_0 = 9.5$ coils. For the sake of verification, experiments with several helices with different radii and pitches were also carried out. Fig. 1(a) shows the experimental setup where the rod is clamped in a mandrel at each end. The upper mandrel is fixed under a rotational stage and the lower mandrel is fixed on a torque-meter, which is attached to a precision scale. The full system (torque-meter+scale+lower mandrel) is fixed to a translation stage allowing vertical translation. The axes of the rotational stage, the mandrels, the helical rod, and the torque-meter all coincide with the vertical.

We note θ the angle between the tangent vector of the rod and the vertical axis and z the vertical end-to-end distance, see Fig. 1(a). Using L, the total arclength of the rod, we define the normalized elongation of the system $\tilde{z} = z/L$. In the case of a pure helix, we have $\tilde{z} = \cos\theta$ and in its natural state the helix has $\tilde{z}_0 = \cos\theta_0$. The translation device therefore allows to change the value of $\tilde{z}$ between $\tilde{z}_0$ and 1. Similarly, we use the normalized variable $\tilde{n} = n/n_0$ describing the winding state. Upon unwinding $\tilde{n}$ decreases from 1 and subsequent axial torque M and axial force T applied on the lower mandrel are recorded. It is useful to note that, by geometry, the radius R and the pitch P of a helix are related to z and n through $R = L/(2\pi n)\sqrt{1-(z/L)^2}$ and $P = z/n$.

Fig. 2 shows typical results of helix unwinding experiments for three different (fixed) values of $\tilde{z}$. The overall mechanical behaviour of the rod is qualitatively similar at any $\tilde{z}$. The unwinding experiments start at $\tilde{n} = 1$ with $(+)$ chirality. As n decreases, M decreases and the axial force T decreases. At a critical $\tilde{n}$, a snapping transition occurs and a perversion is created at one extremity of the rod. For lower $\tilde{n}$ values, a regime takes place where $(+)$ and $(-)$ helices coexist, connected by a perversion. Within this mixed state $(+/-)$, T increases and M exhibits a pseudo-plateau, the plateau value depending on $\tilde{z}$ and $\tilde{z}_0$. As $\tilde{n}$ is further decreased, the perversion disappears at the opposite end, M decreases again and T continues to increase, but with a steeper slope. This latter regime corresponds to a pure $(-)$ helix with chirality opposite to the natural one. The oscillations in experimental data are finite size effects due to clamping, deviating the helical axis from the vertical axis, about which the torque is measured. We also notice a jump in $M(\tilde{n})$ at the $(+)$ to $(+/-)$ transition, when the perversion appears, which coincides with the snapping event (see supplemental video 1). The jump is weaker at the other side of the plateau, when the perversion gets annihilated.

Figure 1(b) shows, in $(\tilde{n}, \tilde{z})$ plane, domains of existence for the states $(+)$, $(-)$ and the mixed state $(+/-)$ where the systems comprises both the $(+)$ and $(-)$ states together with the perversion at the interface between them. The boundary between the different phases in the $(\tilde{n}, \tilde{z})$ plane is determined experimentally in the following way. Instead of keeping $\tilde{z}$ fixed, we found out that following vertical lines in the $(\tilde{n}, \tilde{z})$ plane was easier : we changed z instead of n. The rod was prepared in the coexistence regime for a given $\tilde{n}$, and $\tilde{z}$ was increased. As the rod was elongated, the perversion disappeared (with a corresponding slope discontinuity on the axial torque) for a given $\tilde{z}$, yielding either the pure $(+)$ or $(-)$ state, depending on the sign of $\tilde{n}$. As depicted in Fig. 1(b), the size of the coexistence zone in terms of $\tilde{n}$, decreases as z gets larger, meaning that the more elongated the helix is, the more one needs to unwind to inject a perversion. In the limit where $\tilde{z} \to 1$, the value of $\tilde{n}$ at which the perversion appears goes to 0 : for a completely straight rod, a perversion cannot exist. On the other hand, as $\tilde{z}$ goes down to $\tilde{z}_0$, extrapolation of our experimental data would suggest that any n between $-n_0$ and n_0 would be in the coexistence zone.

To reproduce the phase diagram and the profiles of $T(n)$ and $M(n)$ we use a biphasic approximation in which we neglect the perversion and the boundary layers near the clamps, which is equivalent to assuming the limit $n_0 \to \infty$. We therefore work with the elastic energy

$$E(\kappa_\pm, \tau_\pm, \alpha) = \alpha L \epsilon_+ + (1-\alpha) L \epsilon_-, \qquad (1)$$

where α and $(1-\alpha)$ are the contour fractions of rod

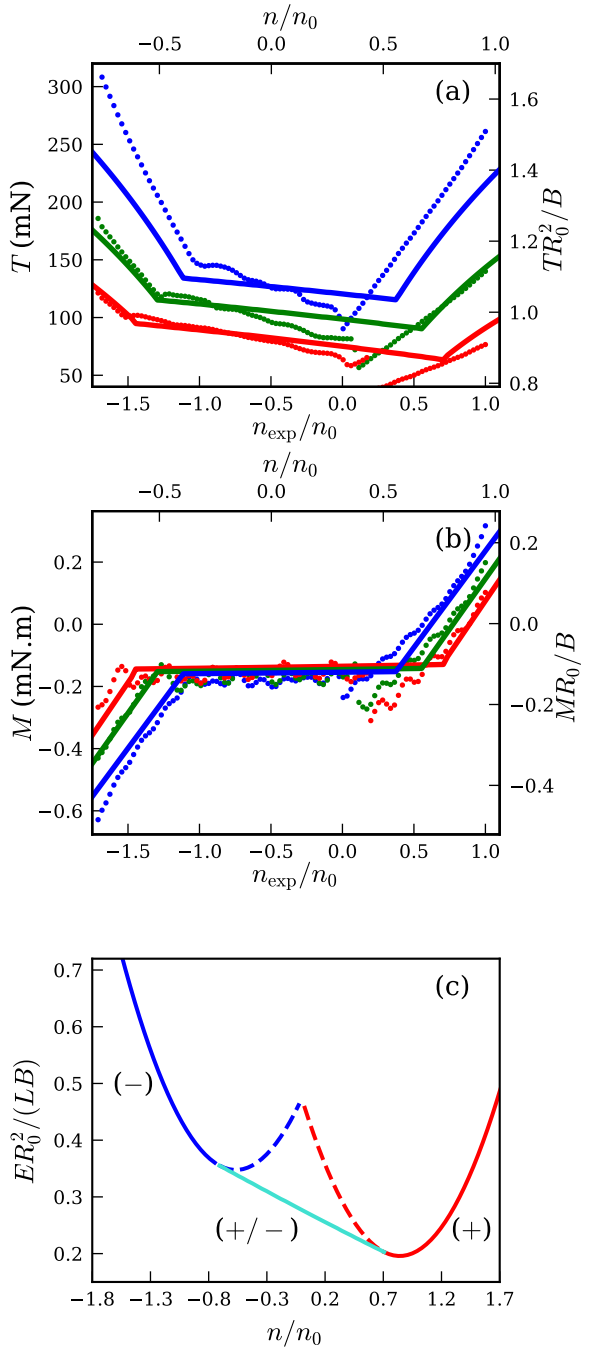

FIGURE 2. Profiles of the force $T(n)$ (a) and torque $M(n)$ (b) for $n_0 = 9.5$ coils and $\tilde{z_0} = 0.2$. Different values of the elongation $\tilde{z}$ are used : blue, $\tilde{z} = 0.93$; green, $\tilde{z} = 0.88$; red, $\tilde{z} = 0.82$. Dots are measured quantities and thick lines are quantities calculated in the biphasic approximation for a rod with Poisson ratio $\nu = 0.5$. c) Strain energy calculated separately for all three phases for $\tilde{z} = 0.82$. The physical solution corresponds to the minimal one at given n.

in the (+) and (−) chirality states respectively. In the Kirchhoff approximation [2, 30], which assumes that the rod is inextensible, unshearable, and has constant cross-section, linear densities of energy $\epsilon_\pm$ write

$$\epsilon_\pm = \frac{1}{2}B\left(\kappa_\pm - \kappa_0\right)^2 + \frac{1}{2}C\left(\pm\tau_\pm - \tau_0\right)^2, \qquad (2)$$

where B and C are the bending and the twisting stiffnesses. For a homogeneous and isotropic material $B = EI$ and $C = EI/(1+\nu)$, where $I = \pi d^4/64$ is the second moment of the circular cross-section, ν the Poisson ratio, and E the Young modulus. The quantities $\kappa_\pm$ and $\tau_\pm$ are respectively the curvature and the torsion in the equilibrium chiral states $\chi = \pm 1$, and κ_0 and τ_0 are their intrinsic values in the rest state. In our notation the torsions $\tau_\pm$ of both (+) and (-) states are positive. Curvatures are related to radii and pitches by $\kappa_i = R_i/(R_i^2 + \frac{P_i^2}{4\pi^2})$ and $\tau_i = \frac{|b_i|}{2\pi}/(R_i^2 + \frac{P_i^2}{4\pi^2})$, where i stands for $+$, $-$ or 0.

The energy (1) is minimized under fixed elongation ζ and winding number μ

$$\zeta = \alpha L\frac{\tau_+}{\sqrt{\kappa_+^2+\tau_+^2}} + (1-\alpha)L\frac{\tau_-}{\sqrt{\kappa_-^2+\tau_-^2}} = z \qquad (3a)$$

$$\mu = \alpha\frac{L}{2\pi}\sqrt{\kappa_+^2+\tau_+^2} - (1-\alpha)\frac{L}{2\pi}\sqrt{\kappa_-^2+\tau_-^2} = n. \qquad (3b)$$

The conformation of the rod at given z and n is then found by introducing the Lagrangian

$$\mathcal{L} = E - T(\zeta - z) - 2\pi M(\mu - n)$$

where T and M are the lagrange multipliers associated with the constraints (3), and are recognized as the axial force and axial torque applied on the system. This variational approach has then seven unknowns : $\kappa_\pm$, $\tau_\pm$, α, T, and M. Requiring $\partial\mathcal{L}/\partial\kappa_\pm = 0$ and $\partial\mathcal{L}/\partial\tau_\pm = 0$ yields

$$\frac{T}{B} = \gamma_+\tau_+\sqrt{\kappa_+^2+\tau_+^2} = \gamma_-\tau_-\sqrt{\kappa_-^2+\tau_-^2}\,, \qquad (4a)$$

$$\frac{M}{B} = (\kappa_+^2+\tau_+^2)^{-1/2}\left[\kappa_+(\kappa_+-\kappa_0) + \Gamma\tau_+(\tau_+-\tau_0)\right] \qquad (4b)$$

$$= -(\kappa_-^2+\tau_-^2)^{-1/2}\left[\kappa_-(\kappa_--\kappa_0) + \Gamma\tau_-(\tau_-+\tau_0)\right]\,, \qquad (4c)$$

where we have used the notations $\gamma_\pm = \kappa_0/\kappa_\pm - 1 + \Gamma(1 \mp \tau_0/\tau_\pm)$ and $\Gamma = C/B = 1/(1+\nu)$. These equations (4) corroborate the conservation of force T and torque M along the rod, and are equivalent to the conserved quantities $I_2 \equiv \mathbf{T}^2$ and $I_3 \equiv \mathbf{M}\cdot\mathbf{T}$ [30], with $\mathbf{T} = (0, 0, T)$ and $\mathbf{M}\cdot\mathbf{T}/T = M$.

In the cases $\alpha = 0$ or $\alpha = 1$, corresponding to purely (+) and (−) configurations, $\kappa_\pm$ and $\tau_\pm$ are found from (3). The loads T and M are given by (4), and the energy by (1). When computing the profiles of Fig. 2, we need to compared the energy of the purely (+) and (−) states to

the energy of the mixed state, i.e. when $0 < \alpha < 1$. The value of α is fixed by setting $\partial\mathcal{L}/\partial\alpha = 0$ which yields

$$\kappa_+^2 + (\Gamma + 2\gamma_+)\tau_+^2 = \kappa_-^2 + (\Gamma + 2\gamma_-)\tau_-^2 \ , \qquad (5)$$

which is, interestingly, equivalent to conservation of the invariant $I_1 \equiv \kappa_1^2 + \kappa_2^2 + \Gamma\kappa_3^2 + 2\mathbf{T}\cdot\mathbf{d_3}/B$, with $\mathbf{d_3}$ the tangent to the rod [32].

The seven equations (3), (4) and (5) are solved numerically for the seven unknowns. For the mixed state, we only keep solutions having $0 < \alpha < 1$. For these solutions, the energy is always found to be lower than the energy of the pure (+) and (−) states : as soon as it exists the mixed state prevails. The phase diagram of Fig. 1(b) is drawn for $z_0 = 0.2$ and shows for which values of $\tilde{z}$ and $\tilde{n}$ each of the three states ((+), (−), or mixed) prevails. The red line corresponds to either $\alpha = 0^+$ or $\alpha = 1^-$ and represents the calculated boundary in $(\tilde{z}, \tilde{n})$ plane at which the mixed state becomes energetically favourable. The blue line represents the occurrence of $z_- = 0$ within the mixed phase. Below this line the solution has $z_- < 0$, indicating that the load on the (−) coil is not sufficient to extend it. Consequently, this (−) coil remains in self-contact during experiments. Corresponding calculated profiles $M(\tilde{n})$ and $T(\tilde{n})$ are shown on Fig. 2.

The model captures the overall features found in experiments : a decrease in axial torque upon unwinding, followed by a pseudo plateau in the phase coexistence regime, concluded by a total inversion of chirality, with a further decrease of the axial torque. Its average value on the pseudo plateau is approximately $M_{\text{plateau}} \approx -B\Gamma\,\tilde{z}\tilde{z}_0\sqrt{1-\tilde{z}_0^2}/R_0$ while deviation from this constant is $\Delta M \equiv M(\alpha = 1^-) - M(\alpha = 0^+) \approx 2.5B\Gamma(1-\tilde{z})\tilde{z}_0^2/R_0$, indicating that for $\tilde{z}$ close to 1 and $\tilde{z}_0$ small (weak natural torsion), the slope of the plateau can be neglected comparing to M_{plateau}. In our case $\tilde{z}_0 = 0.2$ and for $\tilde{z} > 0.8$ we have $M_{\text{plateau}}/\Delta M \gtrsim 10$. Therefore, in what follows we omit the prefix "pseudo" and use the term "plateau". Notice that M_{plateau} scales with the twisting stiffness C and $\tilde{z}_0$, related to τ_0 via $\tilde{z}_0 = \tau_0/\sqrt{\kappa_0^2 + \tau_0^2}$. This means that during inversion one has to provide work against the natural torsion of the helix in order to inverse the pitch. When $z/L \to 1$ the transition line (red line on Fig. 1) can be computed analytically to be $\tilde{z} \approx 1 - (1/2)(\tilde{n}\Gamma/\sin\theta_0)^2$. The corresponding force at transition reads $T \approx B(1-\tilde{z_0}^2)^2/(\Gamma R_0^2)$ and the torque $M \approx -B\Gamma\tilde{z}_0\sqrt{1-\tilde{z_0}}/R_0$. These formulas remind us that transition at $z = L$ (usually called the *writhing* transition) happens at *finite* loads, and generalize the critical load values for the existence of a perversion given in [30].

The overall behaviour on the calculated axial force T also reproduces the experimental trends. Yet, there is a shift in the value of $\tilde{n}$ between experiment (upper abscissa labels) and theory (lower abscissa labels), shown on Fig. 2. This shift is a manifestation of some memory effects that our theory, based on linearly elastic and unshearable rods, does not capture. The memory effects can be avoided if one chooses vertical trajectories in (n, z) space as we did for constructing the phase diagram, Fig. 1(b).

We now focus on experimental features not captured by the biphasic approximation. The jumps in M at the injection and expulsion of the perversion are absent in the biphasic approximation. The surplus of axial torque necessary to inject the perversion is due to the energy barrier necessary for the nucleation of the perversion. The analytical biphasic model does not take into account this energy barrier, and this explains why the values of $\tilde{n}$ at which the perversion appears do not concur on Fig. 1(b) and Fig. 2 : one has to unwind further in order to provide enough energy to overcome the nucleation energy barrier. Moreover, depending on $\tilde{z}$, the snapping occurring at the creation of a perversion is accompanied by a self-contact within the first coil, see supplemental video 1. The jump in M at the disappearance of the perversion is far less pronounced : indeed, the left side of experimental and theoretical profiles coincide fairly on Fig. 1(b) and Fig. 2(b). Another feature not reproduced by the biphasic approximation are the oscillations in $M(n)$, related to finite size and boundary effects.

In order to capture the finite-size effects due to the perversion and the boundaries, we carried out numerical simulations of a Kirchhoff elastic rod. The Kirchhoff rod theory uses the center line $\mathbf{r}(s)$, the arclength s, and the local orthonormal frame $(\mathbf{d_1}(s), \mathbf{d_2}(s), \mathbf{d_3}(s))$ to keep track of the spatial deformation of the rod. In the present unshearable and inextensible case, $\mathbf{d_3}(s)$ is the tangent to the rod

$$\mathbf{r}'(s) = \mathbf{d_3}(s) \qquad (6)$$

At equilibrium, the deformation of the rod is due to external forces $\mathbf{f_{ext}}$ and moments $\mathbf{m_{ext}}$ which are balanced by the internal force $\mathbf{T}(s)$ and internal moment $\mathbf{M}(s)$

$$\mathbf{T}'(s) + \mathbf{f_{ext}} = 0 \qquad (7a)$$

$$\mathbf{M}'(s) + \mathbf{r}' \times \mathbf{T} + \mathbf{m_{ext}} = 0 \qquad (7b)$$

The internal force and moment are linked to the deformation fields $\kappa_1(s), \kappa_2(s), \kappa_3(s)$ by constitutive relations

$$\mathbf{M}(s)\cdot\mathbf{d_i}(s) = B_i\ (\kappa_i(s) - \kappa_{i0}(s)) \qquad (8)$$

where the $\kappa_{i0}(s)$ describe the natural shape of the rod (uniform when this natural shape is helical). The curvatures $\kappa_1(s), \kappa_2(s)$ and twist $\kappa_3(s)$ control how the material frame $(\mathbf{d_1}(s), \mathbf{d_2}(s), \mathbf{d_3}(s))$ warps along the rod

$$\mathbf{d_i}'(s) = \kappa_i \times \mathbf{d_i}(s) \qquad (9)$$

In the present case where the rod material is uniform and isotropic, and the section of the rod is circular, we have $B_1 = B_2 = B = EI$ and $B_3 = C = EI/(1+\nu)$. The rod is clamped at both ends and, for given n

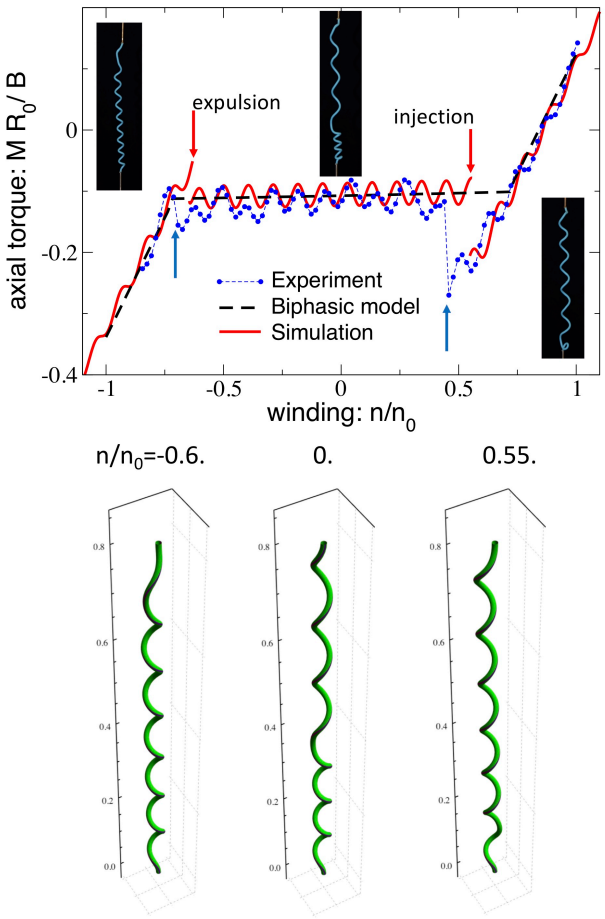

FIGURE 3. Experimental profile $M(n)$ compared to numerical result and biphasic calculation. The parameters for simulation are $\tilde{z}_0 = 0.2$, $\tilde{z} = 0.82$, $n_0 = 9.5$. The events of creation and annihilation of the perversion are pointed by arrows, blue for experiment and red for simulation. The snapshots of the rod at these events and in the mixed state are shown in insets. Calculated configurations for the three cases are shown on the lower panel.

and z, the full system (6), (7), (8), (9) is solved with a boundary value problem software (in the present case AUTO07p [33]). For each equilibrium, we keep track of the axial force T and axial torque M applied on the rod by the clamps and use pseudo-arclength continuation to follow the changes in the equilibrium as n is varied. The simplified biphasic model presented above correspond to a solution with uniform curvatures and twist

$$\kappa_1 = \kappa_\pm\,, \quad \kappa_2 = 0\,, \quad \kappa_3 = \pm\tau_\pm \tag{10a}$$

$$\mathbf{T} = (0, 0, T) \tag{10b}$$

$$\mathbf{M}(s) = R_\pm\, T\, \mathbf{e}_\psi + M\, \mathbf{e}_\mathbf{z} \tag{10c}$$

$$\mathbf{r}(s) = R_\pm\, \mathbf{e}_\mathbf{r} + s\, \tilde{z}\, \mathbf{e}_\mathbf{z} \tag{10d}$$

where $(\mathbf{e}_\mathbf{r}(s), \mathbf{e}_\psi(s), \mathbf{e}_\mathbf{z})$ is the rotating cylindrical frame. In the transition regime, when the perversion is present, there are multiple equilibrium branches and we only show the branch with the lowest energy. We also found convenient to add a small amount of gravity (in $\mathbf{f_{ext}}$) in both the axial and transversal directions.

Results for $M(n)$ at fixed elongation $\tilde{z} = 0.82$ is shown on Fig. 3 and compared to both experiments and the biphasic model. The entire simulated n-evolutions of M including the shapes of the clamped rods with $n_0 = 9.5$ and $n_0 = 4$ are shown in supplemental videos 2 and 3 respectively. The discontinuities at injection and expulsion of the perversion are recovered with fair precision, as well as the oscillations. Notice from the videos that the jumps at injection/expulsion and the amplitude of oscillations decrease with increasing n_0, as expected [34]. Furthermore, we see that the asymmetry between the creation and annihilation jumps are also reproduced by the simulation. This is expected, since the state of inverse chirality is energetically higher than the original one because of the positive natural chirality of the rod. This results in the asymmetry between injection and expulsion jumps and also in the non-zero value of the plateau in M. Obviously, this asymmetry increases with natural torsion τ_0. Creation of the perversion proceeds via snapping instability, and depending on the applied elongation $\tilde{z}$, this snapping event might be accompanied by a self-contact, as in the case on Fig. 3 and in supplemental video 1.

The oscillations of axial torque during the coexistence regime are linked to the clamping boundary conditions. Recall that in the biphasic model, where conformations are purely helical, these oscillations are absent. Clamping conditions are incompatible with pure helical shapes, as the conformation near the clamp cannot be a helix. Therefore by constraining the rod to be clamped at opposite ends, we introduce some axial asymmetry, which results in the observed oscillations. Notice that the frequency of oscillations during the chirality inversion experiment from n_0 to $-n_0$ is one per turn.

Yet the Kirchhoff model does not reproduce the encountered memory effects, implying that the intensive quantities M and T depend on the history of the system in (n, z) space. The measured profiles $M(n)$ and $T(n)$, see Fig. 2, are obtained by scans from n_0 to $-n_0$, resulting in a shift of n_{exp} with respect to the calculated profile. The memory effects are particularly strong in mixed state (data not shown), indicating that their origin is related to the perversion, where strains are much stronger than within the helices. These are indications that corrections due to non-linearities, shear strain, extensibility or even plastic deformation are to be taken into account for realistic materials [34]. This study is out of frame of the present analysis. The injection of the perversion is analogous of a nucleation event. The existence of a well defined Maxwell-like pseudo plateau corroborates that we deal indeed with a domain wall driven transition. The analogy with phase transition invoking heterogeneous nucleation is an interesting scientific playground. In this sense, the perversion

acts as a boundary between two de-mixed phases. As recently pointed out, the perversion itself can be associated to a soliton-like excitation [22]. This soliton is free to move in a system where two chirality states are degenerate, i.e. for a rod with natural curvature $\kappa_0 > 0$ but no natural torsion $\tau_0 = 0$. The rest state of such rod would be a $n-$circle. Our present analysis assumes both κ_0 and τ_0 to be non-zero, implying that the rest natural state is a positive helix with finite positive pitch, while the inverted helix, when unloaded, has collapsed coils. Thus, the degeneracy between $(+)$ and $(-)$ states is lifted by finite τ_0. A further consequence is that the perversion is not free to move due to the finite plateau value of M. Consequently, the helical rod in the mixed state acts as a *constant torque actuator*, illustrated by the experimental demonstration on supplemental video 4. Moreover, our numerical simulation based on Kirchhoff model demonstrates that even highly nonlinear snapping events, i.e. injection and expulsion of perversion, can be captured by a theory based on linear elasticity only. These controlled snapping events could also be a perspective in robotics aiming to producing rapid mechanical action by continuous drive.

Our findings on this apparently simple mechanical system point out several remarkable features which can be of importance at micro and macro levels, from biological and bio-inspired micro-robotics [35] to mechanical engineering [36] and can bring some new insight even in context of single-molecule unwinding [37]. More generally, torque plateau and injection/annihilation snapping events are remarkable observable phenomena certainly relevant for exploring Nature and for design of new biomimetic devices.

The present research is a part of DynaVine action supported by IDEX grant Emergence from Université Paris Cité. We also would like to thank A. Goriely, L. Truskinovsky, and D. Bigoni for discussions.

* drazen.zanchi@u-paris.fr

[1] G. Kirchhoff, J. Reine Angew. Math. **56**, 285 (1859).
[2] A. E. H. Love, *A treatise on the mathematical theory of elasticity*, 4th ed. (Dover, 1990).
[3] S. P. Timoshenko and J. M. Gere, *Theory of Elastic Stability*, 2nd ed. (McGraw-Hill, 1961).
[4] B. Audoly and Y. Pomeau, *Elasticity and Geometry : From hair curls to the non-linear response of shells* (Oxford University Press, 2010).
[5] A. Goriely, *The Mathematics and Mechanics of Biological Growth* (Springer Nature, 2016).
[6] T. R. Strick, J.-F. Allemand, D. Bensimon, A. Bensimon, and V. Croquette, Science **271**, 1835 (1996).
[7] J. F. Allemand, D. Bensimon, R. Lavery, and V. Croquette, Proceedings of the National Academy of Sciences **95**, 14152 (1998).
[8] Z. Bryant, M. D. Stone, J. Gore, S. B. Smith, N. R. Cozzarelli, and C. Bustamante, Nature **424**, 338 (2003).
[9] A. Sarkar, J.-F. Léger, D. Chatenay, and J. F. Marko, Physical Review E **63**, 051903 (2001).
[10] C. Bustamante and S. Yan, Quarterly Reviews of Biophysics **55**, 1 (2022).
[11] J. F. Marko and S. Neukirch, Phys. Rev. E **88**, 062722 (2013).
[12] D. E. Moulton, T. Lessinnes, and A. Goriely, Journal of the Mechanics and Physics of Solids **142**, 104022 (2020).
[13] A. Goriely and S. Neukirch, Physical Review Letters **97**, 184302 (2006).
[14] T. J. Jones, E. Jambon-Puillet, J. Marthelot, and P. T. Brun, Nature **599**, 229 (2021).
[15] J. Mehling, M. Diftler, M. Chu, and M. Valvo, in *The First International Conference on Biomedical Robotics and Biomechatronics* (IEEE, 2006) pp. 690–695.
[16] V. Lutz-Bueno, S. Bolisetty, P. Azzari, S. Handschin, and R. Mezzenga, Advanced Materials **32**, 2004941 (2020).
[17] A. F. da Fonseca and D. S. Galvão, Physical Review Letters **92**, 175502 (2004).
[18] Z. Zhou, P.-Y. Lai, and B. Joós, Physical Review E **71**, 052801 (2005).
[19] L. Dai and W. Z. Shen, Nanotechnology **20**, 465707 (2009).
[20] L. Dai, K.-D. Zhu, W. Shen, X. Huang, L. Zhang, and A. Goriely, Nanoscale **10**, 6343 (2018).
[21] A. Lazarus, J. Miller, and P. M. Reis, Journal of the Mechanics and Physics of Solids **61**, 1712 (2013).
[22] K. Sun and X. Mao, Phys. Rev. Lett. **127**, 098001 (2021).
[23] C. Darwin, *On the movements and habits of climbing plants* (Cambridge University Press, 1865).
[24] S. J. Gerbode, J. R. Puzey, A. G. McCormick, and L. Mahadevan, Science **337**, 1087 (2012).
[25] R. E. Goldstein, A. Goriely, G. Huber, and C. W. Wolgemuth, Physical Review Letters **84** (2000).
[26] D. Nakane, T. Ito, and T. Nishizaka, Journal of Bacteriology **202**, e00735 (2020).
[27] J. P. Canejo and M. H. Godinho, Materials **6**, 1377 (2013).
[28] P. E. S. Silva, J. L. Trigueiros, A. C. Trindade, R. Simoes, R. G. Dias, M. H. Godinho, and F. V. de Abreu, Scientific Reports **6**, 23413 (2016).
[29] A. Goriely and M. Tabor, Physical Review Letters **80**, 1564 (1998).
[30] McMillen and Goriely, Journal of Nonlinear Science **12**, 241 (2002).
[31] G. Domokos and T. J. Healey, International Journal of Bifurcation and Chaos **15**, 20 (2005).
[32] S. Kehrbaum and J. H. Maddocks, Philosophical Transactions of the Royal Society of London. Series A, Mathematical and Physical Sciences **355**, 2117 (1997).
[33] E. Doedel, H. B. Keller, and J. P. Kernevez, International Journal of Bifurcation and Chaos **1**, 745 (1991).
[34] L. Truskinovsky and A. Vainchtein, Journal of the Mechanics and Physics of Solids **52**, 1421 (2004).
[35] M. Vogt, M. Langecker, M. Gouder, E. Kopperger, F. Rothfischer, F. C. Simmel, and J. List, Nature Physics (2023), 10.1038/s41567-023-01938-3.
[36] A. Afghoul, S. Amaravadi, A. Boumali, J. Calmeto, J. Lima, J. Lovell, S. Tinkham, K. Zemlak, and T. Staal, Oilfield Review **16**, 38 (2004).
[37] J. F. Marko and S. Neukirch, Phys. Rev. E **88**, 062722 (2013).

SUPPLEMENTAL MATERIALS

Fig. S1 shows three helical rods made of elasotmer cited in text. On the left panels the rods are in their natural conformation (+) with some non-zero positive pitch. Right panels show the same rods after chirality inversion by unwinding, in the (−) conformation. These inverted conformations are held by friction and self contact.

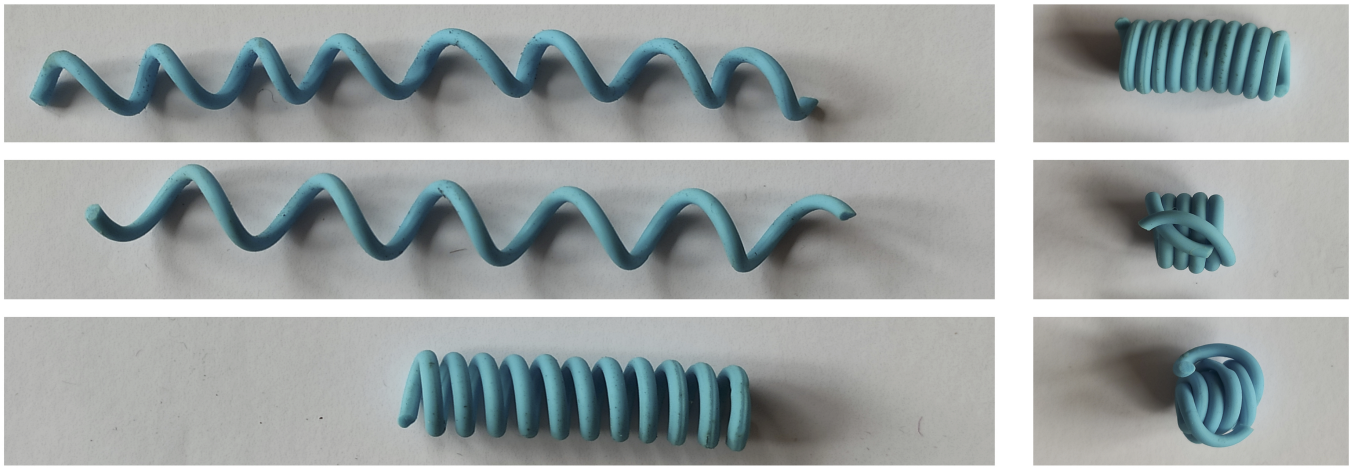

FIGURE S1. Three helices in their natural state with (+) chirality (left panels), and the same helices in their inverted conformations with (-) chirality (right panels).

SUPPLEMENTAL VIDEO 1

The video shows the experiment described in the text : inversion of a helix by continuous unwinding. The parameters are : the unloaded coil radius $R_0 = 3.9$ mm, the pitch $P_0 = 4.7$ mm, the rod thickness $d = 1.7$ mm, the number of coils of unloaded coil $n_0 = 9.5$, the extension of unloaded coil $z_0 = 0.2\,L$ and the working extension $z = 0.82\,L$. At the very end the rod breaks at the upper clamp, allowing it to adopt its unloaded conformation in (−) state : the helix is collapsed and held by self contact between coils.

SUPPLEMENTAL VIDEO 2

Numerical simulation of a helical rod upon continuous unwinding. Parameters were $n_0 = 9.5$, $z_0 = 0.2\,L$, $z = 0.82\,L$ and $\nu = 1/2$.

SUPPLEMENTAL VIDEO 3

Simulation of a $n_0 = 4$ helical rod by continuous unwinding. All other parameters are the same as in Supplemental video 2.

SUPPLEMENTAL VIDEO 4

Demonstration of a constant torque motor. The axial torque is rapidly compensated by viscous drag between the rotating wooden stick and the air. The system is held at constant elongation z by a thin black sewing thread attached on the lower side in the middle of the wooden stick (not visible in video). The thread allows the stick to rotate (almost) freely, but at constant z. These are the very conditions studied in the main text.